

Half-skyrmions and Bimerons in an antiferromagnetic insulator at room temperature

Hariom Jani^{1*}, Jheng-Cyuan Lin², Jiahao Chen², Jack Harrison², Francesco Maccherozzi³, Jonathan Schad⁴, Saurav Prakash¹, Chang-Beom Eom^{4,5}, A. Ariando^{1,6}, T. Venkatesan^{7*}, Paolo G. Radaelli^{2*}

¹Department of Physics, National University of Singapore, Singapore

²Clarendon Laboratory, Department of Physics, University of Oxford, UK

³Diamond Light Source, Harwell Science and Innovation Campus, UK

⁴Department of Materials Science and Engineering, University of Wisconsin-Madison, USA

⁵Department of Physics, University of Wisconsin-Madison, USA

⁶NUS Graduate School for Integrative Sciences and Engineering, National University of Singapore, Singapore

⁷Department of Electrical and Computer Engineering, National University of Singapore, Singapore

In the quest for post-CMOS technologies, ferromagnetic skyrmions and their anti-particles have shown great promise as topologically protected¹⁻⁶ solitonic information carriers in memory-in-logic or neuromorphic devices^{1,7-9}. However, the presence of dipolar fields in ferromagnets, restricting the formation of ultra-small topological textures^{2-4,6,7,10}, and the deleterious skyrmion Hall effect when driven by spin torques^{7,8,10} have thus far inhibited their practical implementations. Antiferromagnetic analogues, which are predicted to demonstrate relativistic dynamics, fast deflection-free motion and size scaling have recently come into intense focus^{7,11-17}, but their experimental realizations in natural antiferromagnetic systems are yet to emerge. Here, we demonstrate a family of topological antiferromagnetic spin-textures in α -Fe₂O₃ – an earth-abundant oxide insulator – capped with a Pt over-layer. By exploiting a first-order analogue of the Kibble-Zurek mechanism^{18,19}, we stabilize exotic merons-antimerons (half-skyrmions⁶), and bimerons^{14,20}, which can be erased by magnetic fields and re-generated by temperature cycling. These structures have characteristic sizes in the range ~ 100 nm that can be chemically controlled via precise tuning of the exchange and anisotropy, with pathway to further scaling. Driven by current-based spin torques from the heavy-metal over-layer, some of these AFM textures could emerge as prime candidates for low-energy antiferromagnetic spintronics at room temperature^{1,7-9,21}.

Topological textures in antiferromagnetic (AFM) materials, which consist of compensated ferromagnetic (FM) sublattices, produce negligible stray fields and possess a net zero *magnetic topological charge*. Nonetheless, the order parameter of AFMs – the Néel vector (\mathbf{L}) – twists in these textures so as to generate a non-zero *Néel topological charge*¹¹. This property endows AFM textures with topological protection, while alleviating the limitations encountered by their FM counterparts^{1,7,11-13}. Furthermore, insulating AFMs are predicted to host ultra-fast spin dynamics and relativistic motion of textures up to \sim few km/s^{11,12,14,22,23} due to low Gilbert damping^{11,22,24} and the exchange amplification effect²³. Lastly, due to negligible Joule losses during magnon-mediated spin transport, AFM insulators are also important candidates for low-power spintronics^{24,25}. Therefore, generating and controlling AFM topological textures in insulators is crucial both for fundamental understanding and applications.

The latest experimental observations of skyrmions in metal-based synthetic AFM stacks have exhibited some of the desirable properties (*e.g.* size scaling and deflection-free motion)^{16,17}; however, equivalent demonstrations in a natural AFM material have been absent. Recently, we discovered that the insulating AFM oxide $\alpha\text{-Fe}_2\text{O}_3$ (hematite), when interfaced with a ferromagnetic over-layer (Co), can support flat (anti)vortices in the AFM layer²⁶. However, these AFM textures, which are *not* equivalent to skyrmions, were nucleated during an irreversible process during sample growth and are unsuitable for some applications due to the inability to provide spin-orbit torques (SOTs) directly at the AFM interface. In contrast, here we demonstrate a variety of AFM topological textures, including analogues of skyrmions, at the interface between $\alpha\text{-Fe}_2\text{O}_3$ and Pt. Furthermore, by varying temperature and doping we show field-free and reversible stabilization of these AFM textures, which can be nucleated below or at room temperature by simple chemical tuning.

$\alpha\text{-Fe}_2\text{O}_3$ crystallizes in the trigonal corundum structure (space group: $R\bar{3}c$), with alternating ferromagnetic sublattices ($\mathbf{M}_{1,2}$) stacked anti-parallel along the c -axis, Fig. 1A (insets). Its spin orientation is governed by the axial magneto-crystalline anisotropy $K(T)$, which varies with temperature due to the delicate interplay between magnetic-dipolar and single-ion interactions^{27,28}. $\alpha\text{-Fe}_2\text{O}_3$ is one of the few systems where $K(T)$ undergoes a sign reversal, causing the spins to reorient across the Morin transition temperature T_M , which can be tuned by chemical substitutions^{28,29}. The Néel vector, $\mathbf{L} \equiv \mathbf{M}_1 - \mathbf{M}_2$, lies *in plane* (IP) above T_M and flips *out of plane* (OOP) below T_M . Above T_M , the presence of a much weaker basal anisotropy term²⁸ results in the formation of six distinct IP \mathbf{L} -domains, *i.e.* three pairs of directional domains, each consisting of elements related by time reversal. For our thin-film $\alpha\text{-Fe}_2\text{O}_3$ samples, grown epitaxially on (0001)-oriented $\alpha\text{-Al}_2\text{O}_3$ substrates by pulsed laser deposition (Methods and Supplementary), the Morin transition occurs at $T_M \sim 240$ K. We also grew Rh-substituted films with the composition $\alpha\text{-Fe}_{1.97}\text{Rh}_{0.03}\text{O}_3$, which display an elevated Morin temperature $T_M \sim 298$ K (see Supplementary)²⁹, due to a strengthened single-ion anisotropy (of spin-orbit origin) relative to the magnetic-dipolar counterpart. The \mathbf{L} reorientation across the respective T_M for these samples was confirmed by X-ray magnetic linear dichroism (XMLD), resonant at the Fe-L edge energies, see Supplementary. Furthermore, when $T > T_M$, a small IP canting (~ 1.1 mrad) occurs between the sublattices $\mathbf{M}_{1,2}$ due to the *bulk* Dzyaloshinskii-Moriya interaction

(DMI)^{30,31}. This canting can be observed in temperature-dependent magnetometry as a small and hysteretic IP moment ($m = M_1 + M_2$) appearing across the Morin transition, Fig. 1A.

To map the spatial distribution of the AFM textures in our samples, we performed XMLD – photo-emission electron microscopy experiments (PEEM) as a function of temperature. Differential energy-contrast images, produced by mapping the quantity $\Delta = (I_{E_1} - I_{E_2}) / (I_{E_1} + I_{E_2})$, were collected using both vertical (LV) and horizontal (LH) linear polarization of the X-rays, incident at a 16° grazing angle onto the films, with the LH polarization axis parallel to the sample plane. The energies E_1 and E_2 are in the shoulders of the Fe- L_{III} double peaks, and were chosen as they are most sensitive to AFM XMLD contrast (Methods)^{26,32}. The PEEM contrast is proportional to the square of the projection of \mathbf{L} onto the X-ray polarization direction (Methods). Qualitatively, considering the grazing incidence of X-rays, the LV (LH) PEEM images are mainly sensitive to the OOP (IP) component of \mathbf{L} , providing a clear identification of the spin reorientation between OOP and IP orientations across the Morin transition. Moreover, within the IP AFM regions, one can combine LH images collected at several different sample azimuthal angles to reconstruct a Néel vector map (phase image of \mathbf{L})^{26,33}, with the caveat that the sign of \mathbf{L} cannot be distinguished by XMLD (Methods).

Fig. 1B-1L show LV-PEEM images of the α -Fe₂O₃–Pt interface at different temperatures while warming through the Morin transition (Methods). For $T < T_M$, Fig. 1B, α -Fe₂O₃ is expected to have mostly OOP spins and indeed we observe large OOP domains (purple regions) separated by AFM anti-phase domain walls – ADWs (yellow boundaries). Although the time-reversed OOP domains produce the same contrast in XMLD, the magnetic sublattices are expected to be reversed by 180° on either sides of the ADWs, so that spins rotate OOP→IP→OOP across the yellow boundary (Supplementary). Upon warming to $T \lesssim T_M$, Fig. 1C-1G, the OOP anisotropy weakens causing the ADWs (containing IP spins) to widen. This is accompanied by nucleation of small IP islands (regions with lighter contrast in Fig. 1C,1D – some examples are encircled in green) emerging in the OOP matrix (purple). Above the transition, $T > T_M$, IP domains dramatically enlarge to become the matrix (yellow regions, Fig. 1H-1L; note that the residual contrast is due to the fact that the X-rays are not perfectly grazing, see Methods), while the remaining OOP islands gradually shrink to become

fine bubbles (small purple dots), which persist up to room temperature. The overall evolution of the AFM textures seen in Fig. 1B-1L can be reversed by cooling the sample across the Morin transition (Supplementary), consistent with a hysteresis of approximately 15 K (seen in the magnetometry results, Fig. 1A). Likewise, at the $\alpha\text{-Fe}_{1.97}\text{Rh}_{0.03}\text{O}_3\text{-Pt}$ interface, we find very similar AFM textures with a temperature evolution that is consistent with T_M being near room temperature, see Supplementary. We also collected images using circular dichroism (XMCD-PEEM, see Methods). These images are completely featureless (Supplementary), indicating that XMCD-PEEM is insensitive to the weak ferromagnetism above T_M , and that the features observed in Fig. 1B-1L are purely of AFM origin.

The IP distribution of \mathbf{L} can be determined from the Néel vector maps generated by combining LH-PEEM images collected at 6 different sample azimuthal angles²⁶ (Methods). In Fig. 2A-2C, the IP orientations of \mathbf{L} are labeled using a red-green-blue (R-G-B) color-scale with 180° periodicity, while OOP orientations are shown as white. At $T < T_M$ (Fig. 2A), most regions have OOP-oriented \mathbf{L} , while the ADWs display an intricate IP winding (R-G-B colors). A detailed analysis reveals the presence of mixed Bloch-/Néel-type domain wall regions (indicated as black and yellow straight lines across the ADWs), whereby the \mathbf{L} rotates in a plane oriented anywhere between *transverse* or *longitudinal* to the domain wall width, respectively (Supplementary). Since a strong *interfacial* DMI (iDMI) would produce spin textures with fixed chirality, as it does at many ferromagnet–heavy-metal interfaces^{15,34,35}, the variation of the chirality along the ADW length in our data is a clear indication that the contribution of iDMI is much weaker than the already weak basal anisotropy. Lastly, our analysis indicates that the small IP islands nucleating inside the OOP matrix have random IP orientations. This nucleation process clearly establishes the first-order nature of the Morin transition.

On warming to $T \sim T_M$, the OOP regions shrink (Fig. 2B), while the ADWs and IP islands widen significantly, sometimes merging with each other if in immediate proximity. Eventually for $T > T_M$ (Fig. 2C), this gives rise to complex AFM textures in which spins are predominantly lying in the basal planes, separated by 60° IP domain walls²⁶. When a region of OOP spins (purple dots, Fig. 2D) happens to be encircled by IP spins with a non-trivial topological winding number (*i.e.*, $w \neq 0$, demarcated as circles or squares in Fig. 2C), the OOP bubble becomes *trapped* and shrinks to a very small size, but does not disappear, since it is topologically forbidden from unwinding completely

into the plane. At these topological pinch-points, the domains merge to form two types of 6-fold pinwheels (R-G*-B-R*-G-B* and R-B*-G-R*-B-G*, asterisk corresponding to time-reversal)²⁶. Around the center of the pinwheels, \mathbf{L} circulates IP either along or against the azimuthal angle, consistent with topologically distinct vortices ($w = +1$) and anti-vortices ($w = -1$). Here, LV-PEEM image (Fig. 2D) measured at the same position as the LH-PEEM based vector map (Fig. 2C) clearly indicates the presence of OOP bubbles trapped at the (anti)vortex cores. This implies that the textures observed in our samples at $T > T_M$ are actually the hitherto unreported AFM *half-skyrmions* (*i.e.* merons, antimerons), containing an OOP AFM core surrounded by whirling IP AFM vortices and antivortices, see schematics in Fig. 2E. The Néel topological charge of the AFM (anti)merons ($Q = \pm 1/2$) depends on both the winding number and the core orientation, so that a core-up meron is topologically equivalent (same charge Q) to a core-down antimeron, see schematics in Supplementary.

The magnetic evolution captured in Fig. 1, 2 as a function of temperature is highly reminiscent of the famous Kibble-Zurek transition^{18,19}, whereby a continuous symmetry is broken across a second-order phase transition. We must, however, point out two key differences: firstly, our system possesses discrete symmetries, rather than continuous ones, though the basal anisotropy breaking the U(1) symmetry is quite weak. Secondly, the Morin transition is first-order, and the formation of topological AFM textures is governed by nucleation rather than fluctuations, as clearly observed in our data (where nuclei coincide with IP islands near T_M). As we previously remarked, the process is completely reversible: *i.e.* the (anti)merons can be destroyed by cooling (see Supplementary) and by application of a magnetic field (discussed below), and recreated by re-warming across T_M . After a complete thermal cycle, the textures almost never re-appear in the same place.

By analyzing the pattern of AFM Néel vectors in Fig. 2C, we can recognise several variants of the two basic topological types (Fig. 2E). Similar to the domain walls at low temperatures, we observe both Néel-type ('hedgehog') and Bloch-type ('vortex') merons, which are topologically equivalent by rotations in spin space, as well as antimerons, which combine these characteristics in their different sectors. Once again, we emphasize that the simultaneous presence of Néel- and Bloch-type objects indicates that the iDMI does not influence the formation of AFM topological textures in our samples. Of further interest is the presence of numerous AFM meron-antimeron pairs (*i.e.*

AFM bimerons — another hitherto unobserved quasi-particle). Some bimerons have extremely small inter-core distances ($\sim 100\text{-}150$ nm) and may have unfractionalized topological charge, since the surrounding IP structure is resolution-limited in LH-PEEM (dashed-black ellipses in Fig. 2C, 2E), while the bimerons consisting of more distant core pairs are probably the topologically fractionalized counterparts³⁶ (see Supplementary). The total topological charge of a bimeron is an integer, such that $Q = \pm 1$ bimerons (a core-up meron plus a core-down antimeron, or vice versa, Supplementary) are topologically equivalent to skyrmions^{14,20,36}, and are important for applications as they allow better 3D race-track stackability²⁰. In contrast, $Q = 0$ bimerons are topologically trivial, but are interesting for applications as they carry a net core L . Crucially, the total winding number away from the cores is *zero* for both $Q = 0$ and $Q = \pm 1$ bimerons, so that like skyrmions but *unlike* isolated (anti)merons, these bimerons can exist in a uniform AFM background (see Supplementary) — potentially an important feature for constructing race-tracks. Topological charges cannot be determined directly from our data due to the sign ambiguity in XMLD (see Methods). Nonetheless, we observe that (anti)merons which had formed separately, but were accidentally located nearby, can either undergo annihilation (black ellipses, Fig. 1H, 1I), or may come closer together and remain stable (red ellipses in Fig. 1J-1L and dashed-black ellipses in Fig. 2C). It is possible that the former could be $Q = 0$ bimerons, which are not fully topologically protected, while the latter are $Q = \pm 1$ bimerons.

One key observation from Fig. 1B-1L is that the feature size of the AFM textures (*i.e.*, ADW widths and (anti)meron cores) is strongly temperature dependent, and diverges at T_M . These sizes are controlled by the competition between the exchange stiffness (A_{ex}) and the anisotropy (K) (known from the literature²⁷⁻²⁹), and are expected to diverge when $|K| \rightarrow 0$. Based on simple analytical ansatz of linear AFM ADWs and linear (anti)merons, we obtained the following expressions for the ADW width (W , when $T < T_M$), and the (anti)meron cores (D , when $T > T_M$), see Methods,

$$\begin{aligned}
 W &= \sqrt{\frac{2\pi^2 A_{ex}}{K}}, \\
 D &= \frac{4}{3} \sqrt{\frac{2\pi^2}{(\pi^2 - 4)} \frac{A_{ex}}{|K|}}.
 \end{aligned}
 \tag{1}$$

In the absence of iDMI, these formulae hold irrespective of the textures' Bloch- or Néel-character. The results of these models, are in good agreement with experimental data extracted from PEEM, as shown in Fig. 3 for both $\alpha\text{-Fe}_2\text{O}_3\text{-Pt}$ and $\alpha\text{-Fe}_{1.97}\text{Rh}_{0.03}\text{O}_3\text{-Pt}$ interfaces. Near T_M , both W and D diverge as $|K| \sim 0$. However, away from T_M , as the magnitude of K increases, both W and D decrease asymptotically. This demonstrates that it is possible to tune the room-temperature size of (anti)meron cores by either reducing A_{ex} or instead increasing $|K|$, noting that the latter would also reduce T_M . Furthermore, the minimal intra-bimeron core-core distance should also be controllable by similar means. The possibility of manipulating meron core sizes either by chemical doping or by exploiting the additional anisotropy induced by an over-layer is of significant interest for practical applications.

Lastly, we study the effect of magnetic fields on the (anti)merons and bimerons. We applied *ex situ* IP magnetic fields and imaged the sample in remanence by LV-PEEM (Fig. 4). The initial zero-field state at room temperature had an (anti)meron number density of $n = 0.45 \pm 0.07 \mu\text{m}^{-2}$, which remains unaffected within error ($\sim 0.41 \mu\text{m}^{-2}$) after application of a 50 mT field, Fig. 4B. Errors are experimental s.d. obtained from multiple images. However, after 500 mT, we found large-scale annihilation of the (anti)merons, with very few surviving textures ($n = 0.01 \pm 0.02 \mu\text{m}^{-2}$), Fig. 4C. This field 'erasability' may result from the movement of the IP domains under the influence of the Zeeman coupling between the field and the IP canted moment (\mathbf{m}). After field erasure, the (anti)merons and bimerons were re-generated by thermally cycling the sample across T_M , Fig. 4D. In this state $n = 0.43 \pm 0.04 \mu\text{m}^{-2}$, which is very similar to the original density. Crucially, the AFM topological textures are reproduced throughout the sample, as confirmed by our large-area measurements (see Supplementary). Hence, in $\alpha\text{-Fe}_2\text{O}_3$ and its derivative systems, the Kibble-Zurek-like phenomenology occurring across the Morin transition can be used as a reversible handle for annihilation and re-generation of AFM (anti)merons and bimerons.

Our results raise an important question: given that currents in the Pt layer are expected to result in spin accumulation at the $\alpha\text{-Fe}_2\text{O}_3\text{-Pt}$ interface via spin Hall effect (SHE), can some of the objects in the AFM topological family be manipulated via SOTs? Recent results^{37,38} of SHE-based IP domain switching in $\alpha\text{-Fe}_2\text{O}_3$ suggest that this may become possible. Furthermore, conceiving

the topological textures as a combination of domain walls, such motion is predicted to be ultra-fast, while being explicitly independent of the iDMI^{14,35}. When realised in practice, such SOT-driven AFM (anti)meron/bimeron motion would open up intriguing possibilities. For example, current-based relativistic motion of these textures may serve as source of nano-scale high-frequency electro-magnetic radiation^{14,23,35}. Alternatively, these textures could be generated in Rh-doped α -Fe₂O₃ near room temperature by Kibble-Zurek cycling or possibly by optical^{39,40} or electrical¹⁴ stimuli, and be driven electrically via SOTs, thereby serving as information vectors in race-track-based memory and logic implementations^{1,7-9,21}.

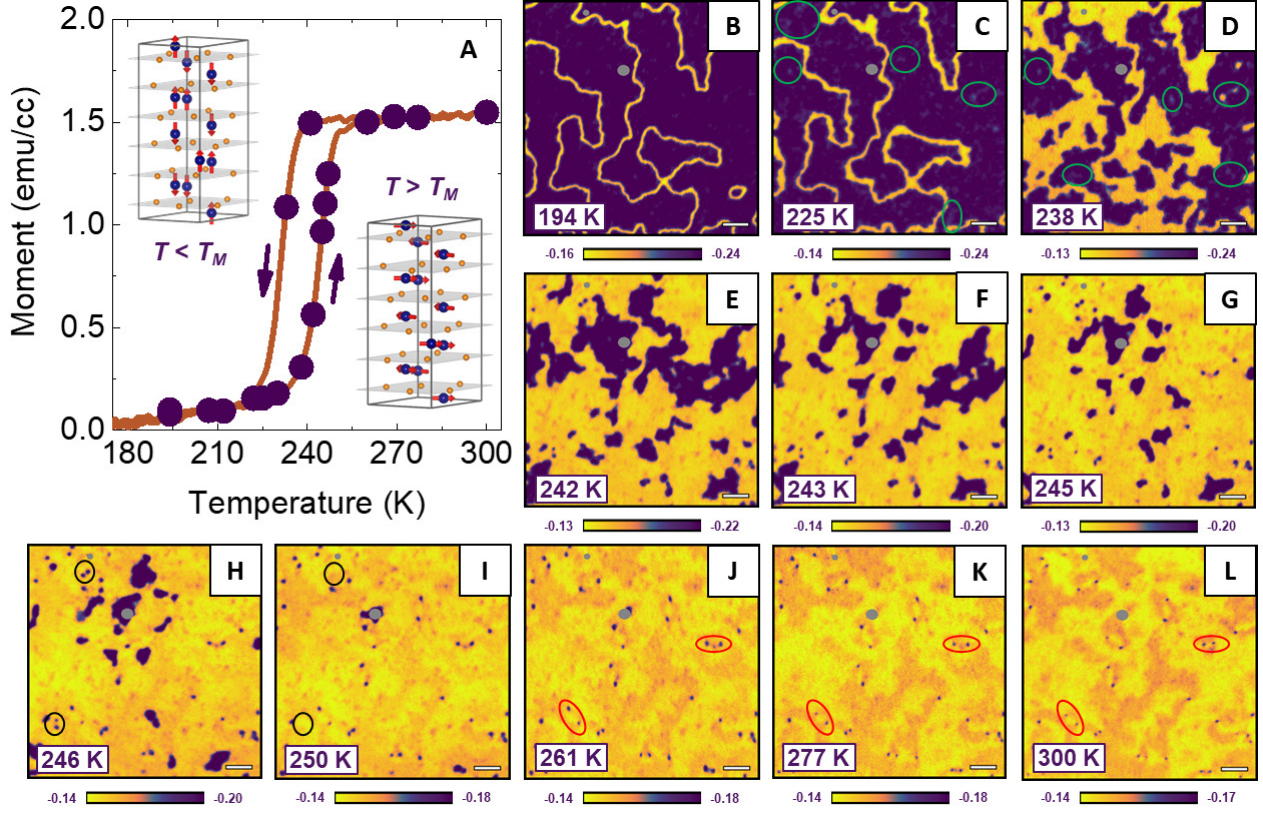


Figure 1. Temperature evolution of AFM textures across T_M in $\alpha\text{-Fe}_2\text{O}_3$. (A) Magnetometry data (brown) of $\alpha\text{-Fe}_2\text{O}_3$ showing hysteresis of the weak net IP moment across the Morin transition, with purple circles indicating PEEM measurement temperatures. Insets show the Fe-spin orientations in the hexagonal unit cell below/above T_M . (B-L) AFM textures in LV-PEEM vs temperature at the $\alpha\text{-Fe}_2\text{O}_3$ –Pt interface, on warming across T_M (cooling sequence in Supplementary). Yellow and purple contrast regions indicate IP and OOP AFM orientations, respectively. Fine purple dots (in H-L) are OOP bubbles, later shown (Fig. 2) to be lying at the core of AFM (anti)merons. All images were recorded at the same position. Energy contrast scales (a.u.), indicated adjacent to each image, were varied slightly across the transition to provide better contrast (Methods). Spatial scale bars are 1 μm . Green ellipses (in C,D) indicate some examples of IP islands in the OOP matrix emerging near T_M . Black ellipses (in H,I) highlight the meron/antimeron pairs that undergo annihilation upon warming. Red ellipses (in J-L) encircle non-annihilating meron/antimeron pairs which are stable and come closer upon warming. The grey regions (in B-L) are defects on the sample surface to focus the PEEM image (Methods).

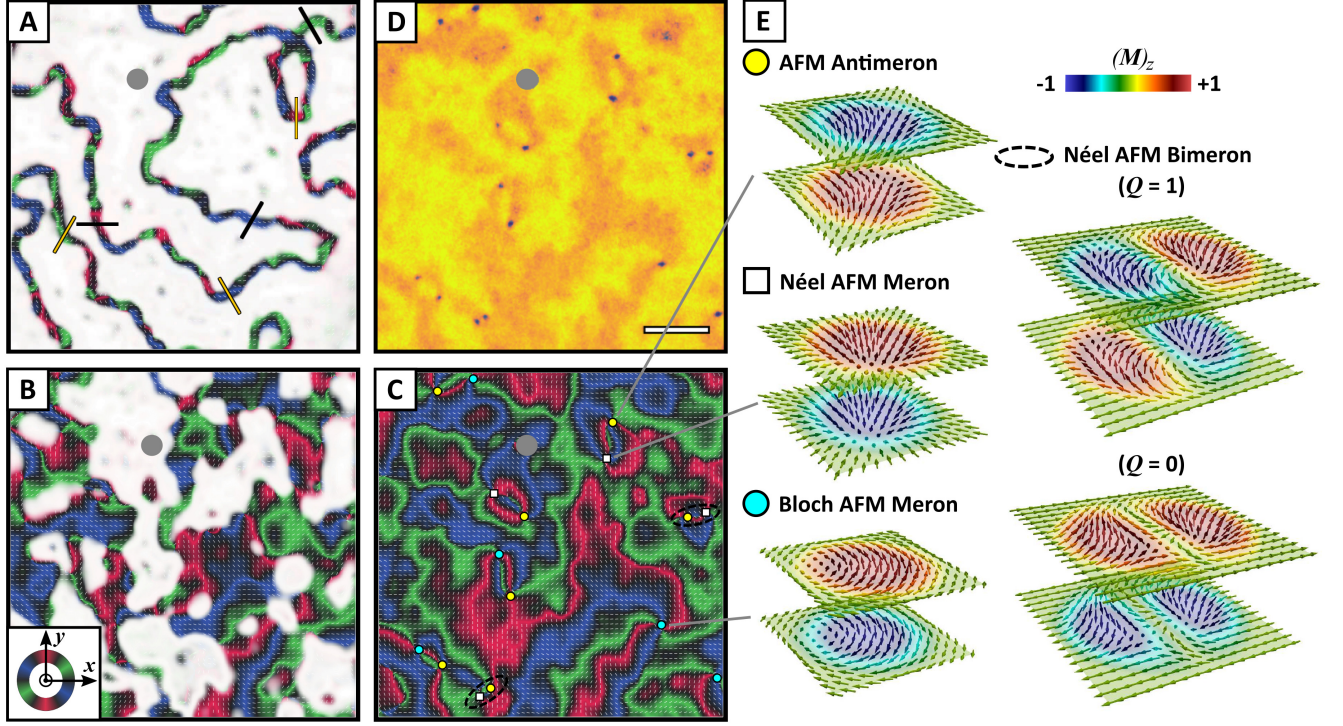


Figure 2. Real-space topological textures from in plane Néel vector maps. Vector-mapped LH-PEEM images at the α -Fe₂O₃–Pt interface, as described in Methods, at (A) $T < T_M$, (B) $T \sim T_M$, and (C) $T > T_M$. R-G-B colors (legend in (B) inset) and thin white bars represent IP L orientations. White regions represent OOP L orientations, and black regions highlight IP L directions deviating significantly from the R-G-B directions. Black and yellow straight lines in (A) demarcate ADW cross-sections with predominantly Bloch- and Néel-type characters, respectively (see Supplementary). (D) LV-PEEM image at the same conditions as in (C) and Fig 1L, showing AFM OOP bubbles lying at the core of the corresponding (anti)vortices in (C). Spatial scale bar is 1 μm long. All images were recorded at the same sample position. The grey regions (in A-D) are defects on the sample surface (see Methods). (E) Schematics of various AFM topological textures demarcated in (C) as circles or squares. Complete topological family shown in Supplementary. The color legend in (E) corresponds to the OOP spin component of the two magnetic sublattices.

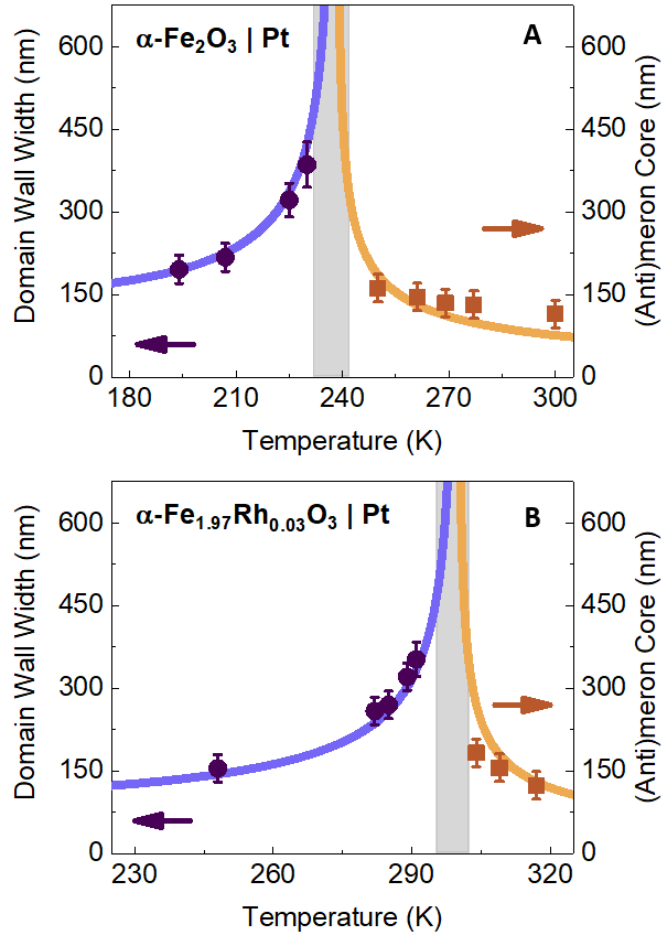


Figure 3. Temperature evolution of AFM feature sizes in (A) $\alpha\text{-Fe}_2\text{O}_3$ and (B) $\alpha\text{-Fe}_{1.97}\text{Rh}_{0.03}\text{O}_3$.

The purple and orange lines are the calculated AFM texture dimensions, W and D , as a function of temperature based on our analytical models (see Methods and Supplementary). Purple circles and orange squares represent corresponding averaged experimental results of ADW widths and (anti)meron core sizes, respectively, extracted from the LV-PEEM images. Error bars represent either experimental standard deviation or PEEM resolution limit, whichever is larger. The zones demarcated as grey are within the Morin transition region where we do not provide experimental data points, since the definition of ADWs and (anti)merons breaks down and all structures become very large.

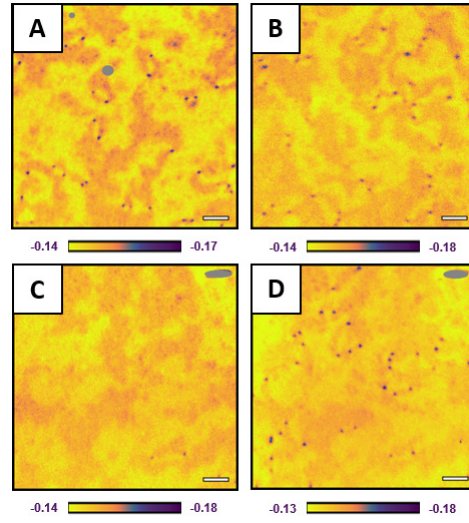


Figure 4. Erasing and re-creating (anti)merons. Room temperature LV-PEEM images at α - Fe_2O_3 –Pt interface in (A) its original state, and in its remanent state after application of (B) 50 mT and (C) 500 mT *ex situ* IP magnetic fields. (D) Final state after the sample in state (C) was thermally cycled (cooling then warming) across T_M . Images (A,B,C) were recorded in different locations on the sample, whereas images (C,D) were recorded at the same position. Spatial scale bars are 1 μm long. The grey regions are defects (see Methods).

References

- ¹ Christian, H. B. *et al.* The 2020 skyrmionics roadmap. *Journal of Physics D: Applied Physics* (2020).
- ² Kurumaji, T. *et al.* Skyrmion lattice with a giant topological hall effect in a frustrated triangular-lattice magnet. *Science* **365**, 914–918 (2019).
- ³ Woo, S. *et al.* Observation of room-temperature magnetic skyrmions and their current-driven dynamics in ultrathin metallic ferromagnets. *Nature Materials* **15**, 501–506 (2016).
- ⁴ Soumyanarayanan, A. *et al.* Tunable room-temperature magnetic skyrmions in Ir/Fe/Co/Pt multilayers. *Nature Materials* **16**, 898–904 (2017).
- ⁵ Nayak, A. K. *et al.* Magnetic antiskyrmions above room temperature in tetragonal heusler materials. *Nature* **548**, 561–566 (2017).
- ⁶ Yu, X. Z. *et al.* Transformation between meron and skyrmion topological spin textures in a chiral magnet. *Nature* **564**, 95–98 (2018).
- ⁷ Büttner, F., Limesch, I. & Beach, G. S. D. Theory of isolated magnetic skyrmions: From fundamentals to room temperature applications. *Scientific Reports* **8**, 4464 (2018).
- ⁸ Zhang, X. *et al.* Skyrmion-electronics: writing, deleting, reading and processing magnetic skyrmions toward spintronic applications. *Journal of Physics: Condensed Matter* **32**, 143001 (2020).
- ⁹ Grollier, J. *et al.* Neuromorphic spintronics. *Nature Electronics* (2020).
- ¹⁰ Litzius, K. *et al.* Skyrmion hall effect revealed by direct time-resolved x-ray microscopy. *Nature Physics* **13**, 170–175 (2017).
- ¹¹ Barker, J. & Tretiakov, O. A. Static and dynamical properties of antiferromagnetic skyrmions in the presence of applied current and temperature. *Physical Review Letters* **116**, 147203 (2016).

- ¹² Baltz, V. *et al.* Antiferromagnetic spintronics. *Rev. Mod. Phys.* **90**, 015005 (2018).
- ¹³ Zhang, X., Zhou, Y. & Ezawa, M. Magnetic bilayer-skyrmions without skyrmion hall effect. *Nature Communications* **7**, 10293 (2016).
- ¹⁴ Shen, L. *et al.* Current-induced dynamics and chaos of antiferromagnetic bimerons. *Physical Review Letters* **124**, 037202 (2020).
- ¹⁵ Caretta, L. *et al.* Fast current-driven domain walls and small skyrmions in a compensated ferrimagnet. *Nature Nanotechnology* **13**, 1154–1160 (2018).
- ¹⁶ Dohi, T., DuttaGupta, S., Fukami, S. & Ohno, H. Formation and current-induced motion of synthetic antiferromagnetic skyrmion bubbles. *Nature Communications* **10**, 5153 (2019).
- ¹⁷ Legrand, W. *et al.* Room-temperature stabilization of antiferromagnetic skyrmions in synthetic antiferromagnets. *Nature Materials* **19**, 34–42 (2020).
- ¹⁸ Kibble, T. W. B. Topology of cosmic domains and strings. *J. Phys. A: Math. Gen.* **9**, 1387–1398 (1976).
- ¹⁹ Zurek, W. H. Cosmological experiments in superfluid helium? *Nature* **317**, 505–508 (1985).
- ²⁰ Göbel, B., Mook, A., Henk, J., Mertig, I. & Tretiakov, O. A. Magnetic bimerons as skyrmion analogues in in-plane magnets. *Physical Review B* **99**, 060407 (2019).
- ²¹ Liang, X. *et al.* Antiferromagnetic skyrmion-based logic gates controlled by electric currents and fields. *arXiv preprint arXiv:1909.10709* (2019).
- ²² Kampfrath, T. *et al.* Coherent terahertz control of antiferromagnetic spin waves. *Nature Photonics* **5**, 31–34 (2011).
- ²³ Galkina, E. G., Galkin, A. Y., Ivanov, B. A. & Nori, F. Magnetic vortex as a ground state for micron-scale antiferromagnetic samples. *Physical Review B* **81**, 184413 (2010).
- ²⁴ Lebrun, R. *et al.* Tunable long-distance spin transport in a crystalline antiferromagnetic iron oxide. *Nature* **561**, 222–225 (2018).

- ²⁵ Wang, Y. *et al.* Magnetization switching by magnon-mediated spin torque through an antiferromagnetic insulator. *Science* **366**, 1125–1128 (2019).
- ²⁶ Chmiel, F. P. *et al.* Observation of magnetic vortex pairs at room temperature in a planar α -Fe₂O₃/Co heterostructure. *Nature Materials* **17**, 581–585 (2018).
- ²⁷ Artman, J. O., Murphy, J. C. & Foner, S. Magnetic anisotropy in antiferromagnetic corundum-type sesquioxides. *Physical Review* **138**, A912 (1965).
- ²⁸ Besser, P. J., Morrish, A. H. & Searle, C. W. Magnetocrystalline anisotropy of pure and doped hematite. *Physical Review* **153**, 632–640 (1967).
- ²⁹ Coey, J. M. D. & Sawatzky, G. A. A study of hyperfine interactions in the system (Fe_{1-x}Rh_x)₂O₃ using the mossbauer effect (bonding parameters). *Journal of Physics C: Solid State Physics* **4**, 2386 (1971).
- ³⁰ Dzyaloshinsky, I. A thermodynamic theory of weak ferromagnetism of antiferromagnetics. *Journal of Physics and Chemistry of Solids* **4**, 241 (1958).
- ³¹ Moriya, T. Anisotropic superexchange interaction and weak ferromagnetism. *Physical Review* **120**, 91–98 (1960).
- ³² Arenholz, E., van der Laan, G., Chopdekar, R. V. & Suzuki, Y. Anisotropic x-ray magnetic linear dichroism at the Fe L_{2,3} edges in Fe₃O₄. *Physical Review B* **74**, 094407 (2006).
- ³³ Waterfield Price, N. *et al.* Coherent magnetoelastic domains in multiferroic BiFeO₃ films. *Phys. Rev. Lett.* **117**, 177601 (2016).
- ³⁴ Luo, Z. *et al.* Current-driven magnetic domain-wall logic. *Nature* **579**, 214–218 (2020).
- ³⁵ Shiino, T. *et al.* Antiferromagnetic domain wall motion driven by spin-orbit torques. *Physical Review Letters* **117**, 087203 (2016).
- ³⁶ Kharkov, Y. â., Sushkov, O. â. & Mostovoy, M. Bound states of skyrmions and merons near the lifshitz point. *Physical Review Letters* **119**, 207201 (2017).

- ³⁷ Zhang, P., Finley, J., Safi, T. & Liu, L. Quantitative study on current-induced effect in an antiferromagnet insulator/pt bilayer film. *Physical Review Letters* **123**, 247206 (2019).
- ³⁸ Cheng, Y., Yu, S., Zhu, M., Hwang, J. & Yang, F. Electrical switching of tristate antiferromagnetic Néel order in α -Fe₂O₃ epitaxial films. *Physical Review Letters* **124**, 027202 (2020).
- ³⁹ Kimel, A. V., Kirilyuk, A., Tsvetkov, A., Pisarev, R. V. & Rasing, T. Laser-induced ultrafast spin reorientation in the antiferromagnet TmFeO₃. *Nature* **429**, 850 (2004).
- ⁴⁰ Khoshlahni, R., Qaiumzadeh, A., Bergman, A. & Brataas, A. Ultrafast generation and dynamics of isolated skyrmions in antiferromagnetic insulators. *Phys. Rev. B* **99**, 054423 (2019).

Supplementary Materials

1. Materials, Methods and Notes: Growth, magnetic and X-ray characterization, Magnetic modelling of ADW width and (anti)meron core size, Exchange stiffness of α -Fe₂O₃.
2. Supplemental Figures: (1) Diffraction and X-Ray Absorption, (2) AFM textures in Rh-doped α -Fe₂O₃, (3) AFM textures in α -Fe₂O₃ during cooling, (4) XMCD-PEEM, (5) Large scale PEEM images, (6) AFM Néel and Bloch ADWs, (7) AFM Néel (anti)merons and bimerons, (8) AFM Bloch (anti)merons and bimerons, (9) Topologically fractionalized AFM bimerons, (10) Exchange interaction terms in α -Fe₂O₃ to calculate exchange stiffness.

Acknowledgments

We would like to thank S. Parameswaran for discussions, F. P. Chmiel for guidance with data reduction, and R. D. Johnson for assistance with experiments. We acknowledge Diamond Light Source for time on Beam Line I06 under Proposals MM23857 and S120317. The work done at University of Oxford (H.J., J.-C.L., J.-H.C., J.H. and P.G.R.) is funded by EPSRC grant no. EP/M2020517/1 (Quantum Materials Platform Grant). The work at National University of Singapore (H.J., S.P., A.A. and T.V.) is supported by National Research Foundation (NRF) under Competitive Research Program

(NRF2015NRF-CRP001-015). A.A. would like to thank the Agency for Science, Technology and Research (A*STAR) under its Advanced Manufacturing and Engineering (AME) Individual Research Grant (IRG) (A1983c0034) for financial support. The work at University of Wisconsin-Madison (J.S. and C.B.E.) is supported by the Army Research Office through Grant W911NF-17-1-0462 and the National Science Foundation under DMREF Grant DMR-1629270.

Author Contributions

H.J. performed material optimization, thin film growth by PLD, structural and magnetic characterization. H.J., J.-C.L., J.H., F.M. performed PEEM experiments. J.-H.C., J.-C.L., H.J. performed data reduction and analysis. J.-C.L., S.P. performed over-layer growth and surface characterization. J.-C.L. assisted in magnetic characterization. J.S. prepared preliminary sputter-grown samples under the supervision of C.-B.E. A.A. and T.V. supervised the PLD film growth and characterization. H.J., under the guidance of P.G.R., prepared the theoretical model. P.G.R. and H.J. conceived the project and supervised the analysis. H.J. and P.G.R. prepared the first draft of the manuscript. All authors discussed and contributed to the manuscript.

*Corresponding authors. Requests for materials and information on supplementary materials should be addressed to H.J. or P.G.R. (emails: hariom.k.jani@u.nus.edu, paolo.radaelli@physics.ox.ac.uk).